Astronomical Techniques and Instruments, 2026

Article Open Access

Design and testing of a high-contrast polarimetric imaging vortex coronagraph

Yutong Cheng[1,2,3], Jiangpei Dou[2,3*], Jing Guo[2,3], Yong Cheng[1]

[1]*College of Electronic and Optical Engineering & College of Flexible Electronics (Future Technology)*, *Nanjing University of Posts and Telecommunications*, *Nanjing* 210023, *China*

[2]*Nanjing Institute of Astronomical Optics & Technology*, *Chinese Academy of Sciences*, *Nanjing* 210042, *China*

[3]*CAS Key Laboratory of Astronomical Optics & Technology*, *Nanjing Institute of Astronomical Optics & Technology*, *Nanjing* 210042, *China*

*Correspondence: jpdou@niaot.ac.cn

Received: ; https://doi.org/10.3724/ati2026014; https://cstr.cn/32083.14.ati2026014

© 2026 Editorial Office of Astronomical Techniques and Instruments, Yunnan Observatories, Chinese Academy of Sciences. This is an open access article under the CC BY-NC-ND 4.0 license (http://creativecommons.org/licenses/by-nc-nd/4.0/)

Citation: Cheng, Y. T., Dou, J. P., Guo, J., et al. 2026. Design and testing of a high-contrast polarimetric imaging vortex coronagraph. *Astronomical Techniques and Instruments*, https://doi.org/10.3724/ati2026014.

Abstract: We propose a high-contrast polarimetric imaging coronagraph based on a vortex phase mask and liquid crystal variable retarders, which takes advantage of the small inner working angle, high throughput, and large discovery area of the vortex coronagraph. This design further improves imaging contrast by incorporating a polarimeter that uses the intrinsic polarization differences between starlight and planetary light. The polarimetric module incorporates two liquid crystal variable retarders operating simultaneously, eliminating the need for manual rotation and enabling both observation and calibration modes. With a single exposure, it allows precise control of linear and circular polarization states and enables full Stokes parameter measurements. Laboratory results demonstrate that the vortex coronagraph achieves an imaging contrast on the order of 10^{-6} at an angular separation of $3\lambda/D$ in the visible band. After integrating the polarimeter, the overall system achieves an imaging contrast of approximately 10^{-9} across the entire image plane at the same angular separation of $3\lambda/D$. This offers significant advantages in enhancing high-contrast imaging performance at small angular distance, and we expect it to provide a feasible technical solution for the direct detection of aged Jupiter-like exoplanets.

Keywords: Direct imaging(2369); Polarimetry(1278); High contrast techniques(2369)

1. INTRODUCTION

Since the discovery of 51 Pegasi b in 1995[1], the number of confirmed exoplanets has exceeded 6,000 to date, detected with various observational techniques. Compared with indirect detection methods, such as radial velocity[2] and transit[3,4], direct imaging provides more comprehensive physical information, including planetary temperature and atmospheric properties. Imaging observations, combined with atmospheric spectroscopy on Earth-like planets located within the habitable zone, also offers the opportunity to detect potential biosignatures beyond the Solar System. However, the brightness contrast between the star and planet poses extreme challenges to direct imaging, with a contrast of up to 10^{-9} required in the visible wavelength to detect aged Jupiter-like planets[5].

The coronagraph technique can effectively suppress the glare of the host star, enabling the detection and analysis of its exoplanets. In recent years, various coronagraph design schemes have been widely proposed and discussed[6]. Among them, the vortex coronagraph proposed by Mawet et al.[7] and Foo et al.[8] and experimentally validated by Guyon[6], is a type of phase mask coronagraph with several advantages, including a small Inner Working Angle (IWA), high throughput, and a large discovery area[9,10]. It works by using the diffraction properties of an optical vortex phase mask[11,12], and includes a Lyot stop to remove unwanted diffracted starlight from the imaging system. Compared with the Four-Quadrant Phase Mask (FQPM) coronagraph[13], the focal-plane vortex phase mask coronagraph avoids the intrinsic blind zones caused by the phase discontinuities at the quadrant boundaries.

In 2008, Swartzlander et al. implemented a scalar vortex coronagraph on a small telescope[14], imaging a binary star system with an angular distance of $1.4\lambda/D$, achieving a 97% suppression of the primary star intensity without affecting the secondary star. With technological

advances, a new manufacturing technique, based on birefringent Liquid Crystal Polymers (LCP), has been developed to create vector optical vortex masks. Based on the Pancharatnam–Berry phase principle[15], these spatially varying birefringent elements generate the vortex phase. In 2010, Mawet et al. created a high-performance vector vortex coronagraph[16], achieving a laboratory contrast on the order of 10^{-5} at $3\lambda/D$ over a 15% bandwidth, with a best result of 2×10^{-6} for a 5% equivalent bandwidth. On-sky observations detected a known brown dwarf with an angular distance of approximately $2.5\lambda/D$ from its host star, with a contrast of about 3×10^{-4}. Another type of vector vortex coronagraph is the Annular Groove Phase Mask (AGPM), created using sub-wavelength diamond gratings. The first science-grade mid-infrared AGPM was produced in 2012[17] and validated on a test bench, demonstrating a raw contrast of approximately 6×10^{-5} at $2\lambda/D$. In recent years, AGPMs have been deployed on several mid-infrared instruments, including the Very Large Telescope (VLT) instruments: VLT Imager and Spectrometer for mid-Infrared (VISIR), NAOS–CONICA (NACO), and Large Binocular Telescope Mid-Infrared Camera (LMIRCam)[18].

The practical performance of coronagraphs is fundamentally limited by speckle noise[19,20]. It has been shown that stellar light and speckle noise are typically unpolarized, whereas light reflected from exoplanetary atmospheres or circumstellar disks shows significant polarization[21]. Therefore, introducing a polarimeter downstream of the coronagraph can further improve the imaging contrast by exploiting the intrinsic polarization differences between the star and the planet. Numerical simulations by Stam et al. demonstrated that the degree of polarization shown by Jupiter-like exoplanets can reach up to approximately 60% at phase angles near 90°[22]. Currently, polarimeters have been used in practical observational systems and have achieved promising results. For example, in 2015, Perrin et al.[23] proposed the design of the polarization measurement mode of the Gemini Planet Imager (GPI) on the Gemini telescope. GPI suppresses non-polarized speckles by a factor of 200, and the Spectro-Polarimetric High-contrast Exoplanet REsearch (SPHERE) instrument / Zurich Imaging Polarimeter (ZIMPOL) on the VLT has achieved a contrast of approximately 10^{-6}[24]. In 2022, Xin et al.[25] from the Yunnan Astronomical Observatory, Chinese Academy of Sciences, developed the single-beam polarimeter at the Cassegrain focus of the 2.4 m Lijiang Telescope. For a target with a V-band magnitude of V = 11.68, the system uncertainty for a 10 s exposure is below 0.8%, enabling high-precision polarization measurements. In 2023, Qiu et al. from the National Astronomical Observatories, Chinese Academy of Sciences, designed a dual-channel polarimetric photometer with time-sequential modulation for the 2.16 m telescope, enabling V-band linear polarimetry and rapid multi-band photometric observations.

In this work, we propose a high-contrast polarimetric imaging coronagraph, based on a vortex phase mask and Liquid Crystal Variable Retarders (LCVRs), with sufficient contrast to achieve approximately 10^{-9} at $3\lambda/D$ across the entire image plane. This system is expected to provide a feasible technical solution for the direct detection of aged Jupiter-like exoplanets.

2. SYSTEM CONFIGURATION AND PRINCIPLE

The polarimetric imaging vortex coronagraph combines high-contrast imaging with full-Stokes polarimetry. The vortex phase mask suppresses on-axis starlight while preserving off-axis signals. Liquid crystal variable retarders provide the phase modulation, and the modulation–demodulation scheme enables reconstruction of the Stokes parameters from intensity measurements.

2.1. Design of the Polarimetric Imaging Vortex Coronagraph

The principal components of our proposed high-contrast imaging system are a vortex-based coronagraph and an LCVR-based polarimeter (see Fig. 1). In the testbed, two laser light sources at a wavelength of 633 nm, output by individual single-mode fibers, are used to simulate stellar and planetary light. The two point light sources are first collimated by lens L1 and then pass through an aperture stop to simulate the entrance pupil, followed by imaging with lens L2. The vortex phase mask is located at the focal plane of lens L2, causing vortex phase modulation of the incident beam, and a Lyot stop is then used to block the diffracted stellar light. The Lyot stop is positioned in a collimated beam path. The beam is re-collimated by lens L3, passes through the Lyot stop, and is subsequently re-imaged by lens L4 to form the coronagraphic focal-plane image. The beam then enters the polarimetric system. After collimation by lens L5, two LCVRs are introduced. By applying controlled voltages, the phase retardance of the LCVRs can be adjusted to modulate the polarization state of the incident light. The modulated beam is subsequently split into two orthogonally polarized components by a Wollaston prism and finally imaged onto a Charge-Coupled Device (CCD) detector via lens L6. The imaging contrast can then be further improved using polarimetry.

The coronagraph modulates the phase of the incident light by introducing a vortex phase mask at the focal plane, redistributing most of the starlight to the outer regions of the pupil. In combination with a Lyot stop, to block this diffracted light, it effectively suppresses the diffraction from the central star. The polarimeter is based around a pair of LCVRs for polarization modulation and a Wollaston prism for dual-beam polarization analysis. The two LCVRs are operated simultaneously, eliminating the need for mechanical rotation for switching the measurement of Stokes Q or U components, which denote the linear polarization states in the Stokes vector. A single expo-

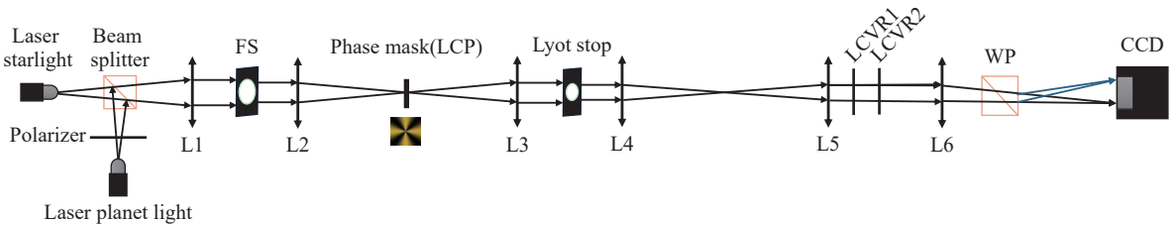


Fig. 1. Optical layout diagram of the vortex polarimetric coronagraph.

sure per modulation state can consequently give precise control of both linear and circular polarization states, allowing measurement of the complete set of Stokes parameters. The system can operate in observation mode and calibration mode. For comparison, Ren et al.[26] proposed in 2019 that combining a vortex coronagraph with a polarimeter could achieve a contrast better than 10^{-11} at small inner working angles in the visible band. Their system employed one LCVR, measuring the polarization of Stokes Q or U by manually changing the fast-axis orientation angle of the LCVR. Our dual-LCVR scheme differs in that it requires no mechanical rotation.

2.2. The Principle of the Vortex Coronagraph

The vortex coronagraph uses a transparent focal-plane phase mask that introduces a helical phase term, $e^{il\theta}$, to the incoming wavefront, where θ is the azimuthal coordinate and l is the topological charge describing the number of helical phase windings imparted by the vortex phase mask. This singular phase structure leads to complete destructive interference at the center, causing the intensity to drop to zero and creating a dark core. The dark core propagates stably along the optical axis and is preserved during transmission[27]. In the ideal case, on-axis starlight is entirely suppressed, but signals from resolvable planets remain unaffected, enabling detection of nearby Earth-sized planets and similar objects.

Optical vortices are characterized by dark channels with destructive interference that nullify coherent light. A single optical vortex at the center of a scalar monochromatic beam, propagating in the z-direction, can be expressed in cylindrical coordinates (ρ, ϕ, z)[28], as

$$E(r,\phi,z) = A(r,z)\exp(il\phi)\exp(-ikz), \tag{1}$$

where $A(r,z)$ is a circularly symmetric amplitude function, $k = 2\pi/\lambda$ is the wavenumber, and l is the topological charge.

2.3. The Principle of the Polarimeter

The key polarization components of the proposed polarimetric system consist of two LCVRs and one Wollaston prism. Traditional mechanical modulation schemes achieve different modulation states by rotating the retarders, but mechanically rotating structures limit the modulation speed and easily cause image motion at the focal plane. With the development of Liquid Crystal (LC) technology, LCVRs acting as electrically tunable wave plates have become a powerful alternative to conventional rotating polarization optics.

The Wollaston prism is primarily used to generate dual beams for polarization modulation, avoiding the need for manual rotation of a polarizer. In this configuration, polarization subtraction processing is not used[29,30]. The polarimetric system adopts a Stokes-balanced modulation scheme. To retrieve the Stokes parameters, four images are recorded under four distinct modulation states. By employing the Imaging Magnetograph eXperiment (IMaX) modulation strategy, the polarization modulation efficiency can be maximized while maintaining the fast-switching capability of the LCVRs[31]. The retardance combinations of LCVR 1 and LCVR 2, corresponding to the four modulation states, are (315°, 305.264°), (315°, 54.736°), (225°, 125.264°), and (225°, 234.736°).

Within the experimental setup, the output Stokes vector, $S_{\rm out}$, is related to the input vector $S_{\rm in}$ by[32], and can be expressed as

$$S_{\rm out} = M_{\rm W} \cdot M_{\rm LCVR2} \cdot M_{\rm LCVR1} \cdot S_{\rm in}, \tag{2}$$

where $M_{\rm LCVR}$ and $M_{\rm W}$ are the Mueller matrices of the LCVRs and the Wollaston prism, respectively.

The Wollaston prism produces two simultaneous orthogonally polarized beams, which correspond to the intensities of the two orthogonal polarization images. Then, by observing the intensities of two orthogonally polarized images in different states, demodulation can yield the four Stokes parameters corresponding to these polarization states.

3. EXPERIMENTAL TESTING AND DISCUSSION

Our study involves comprehensive experimental characterization of the proposed system, including laboratory tests of the vortex coronagraph as well as integrating the polarimeter downstream of the coronagraph. For the polarimeter system, calibration procedures are required, including the retardance calibration of the LCVRs and the calibration of the instrument Mueller matrix.

3.1. The Vortex Coronagraph

For the experimental tests, we used a Thorlabs zero-order LCP vortex half-wave retarder, with a topological charge of $l = 2$ and an operating wavelength of 633 nm, as the vortex phase mask. This was mounted on a three-

axis fine translation stage and positioned at the focal plane to ensure precise alignment between the center of the Point Spread Function (PSF) and the center of the phase mask. We used a Lyot stop, with a diameter of approximately 80% of the original entrance pupil, in the subsequent pupil plane, to block diffracted starlight redistributed outside the geometric pupil. In the vortex coronagraph, the on-axis stellar PSF is modulated at the center of the vortex phase mask. After propagating to the pupil plane, the majority of the on-axis stellar light is diffracted beyond the pupil boundary and then suppressed by the Lyot stop, leaving the off-axis planetary light largely unaffected. We subsequently characterized the performance of the vortex coronagraph through both simulation and experiment. The LCP element functions as a phase plate, with its phase varying azimuthally with the angle θ, described by $e^{il\theta}$, as shown in Fig. 2.

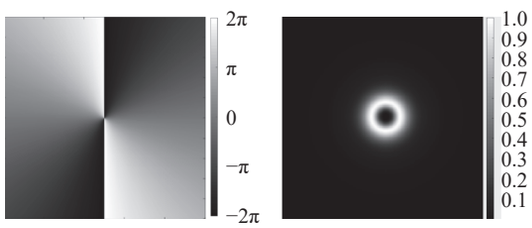


Fig. 2. The phase distribution (Left) and intensity distribution (right) of the $l = 2$ LCP vortex phase mask.

To measure the contrast of the coronagraph, we first record the intensity of the light source without the vortex phase mask. Because the original source intensity was high, we avoided image saturation by using a Neutral Density (ND) filter with an optical density, OD = 4, and a short exposure time of 5 ms. The recorded image corresponds to the original PSF. Subsequently, after aligning the optical path of the vortex coronagraph, we removed the ND filter, and with the same exposure time, we recorded the PSF suppressed by the vortex coronagraph. All images were corrected by subtracting the corresponding averaged dark frames. Where I is the peak intensity of the PSF without the vortex phase mask and I_c is the peak intensity with the vortex phase mask in place, the intensity attenuation, defined as the coronagraphic contrast, is given by I_c/I, with correction applied for attenuation introduced by the ND filter, when applicable. This performance evaluation quantifies the ratio between the maximum intensity of the coronagraphic PSF and that of the non-coronagraphic PSF, characterizing the stellar light suppression capability of the coronagraph[33]. As shown in Fig. 3, the vortex coronagraph achieves a contrast better than 10^{-5} (i.e., on the order of 10^{-6}) at an angular distance of $3\lambda/D$ in the visible wavelength (633 nm).

3.2. LCVR Calibration

The LCVR controls the light beam by altering the retardance through the applied voltage. Consequently, it is necessary to obtain the voltage–retardance calibration data for each LCVR prior to experimentation.

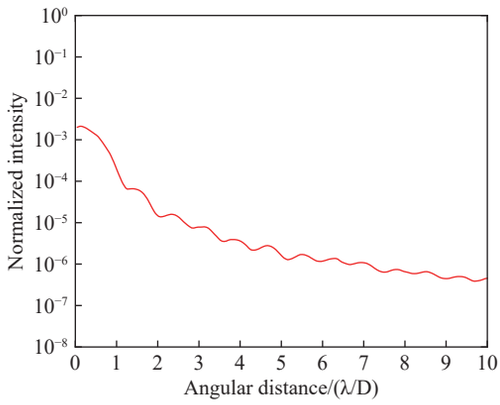


Fig. 3. Experimental contrast curve of the vortex coronagraph. The vortex coronagraph can achieve a contrast of 10^{-6} at an angular distance of $3\lambda/D$ in the visible wavelength (633 nm).

The LCVR to be calibrated is placed between the polarizer and the Wollaston prism, with the fast axis of the LCVR oriented at 45° relative to the reference direction $+Q$. The retardance, δ, can be calculated from the transmitted intensity ratio $I_\perp/I_\parallel$[34], using the relation

$$|\delta| = \begin{cases} N\pi + 2\tan^{-1}\sqrt{\dfrac{I_\perp}{I_\parallel}}, & N = 0,2,4,\cdots \\ (N+1)\pi - 2\tan^{-1}\sqrt{\dfrac{I_\perp}{I_\parallel}}, & N = 1,3,5,\cdots. \end{cases} \tag{3}$$

The retardance, δ, for the extrema of the left and right spot intensities, $I_\perp$ and $I_\parallel$, are integer multiples of π, while the crossing points correspond to half-integer multiples of π. This method is suitable for evaluating the N value. Starting from the high-voltage end, the extrema of $I_\perp$ can be sequentially associated with retardances of π, 2π, 3π, and so on.

In the LCVR calibration, the applied driving voltage ranges from 0 V to 7 V, and the CCD camera is used to acquire images corresponding to each voltage. The calibrated LCVR retardance is then interpolated with a step of 0.001 V, matching the minimum resolution of voltage output. The calibration results of the two LCVRs are shown in Fig. 4. Table. 1 lists the four voltage values required for each LCVR to generate the desired retardance in the polarization modulation.

3.3. Instrument Matrix Calibration

The optical components in the entire system may introduce additional polarization and affect measurement accuracy[35]. Consequently, we employ a calibration unit to calibrate the instrument and determine its Mueller matrix, that is, a linear polarizer and a zero-order quarter-wave plate are inserted into a parallel optical path upstream of the main optical path, acting as the calibration unit. This generates a series of known polarization states as inputs to the system.

The input Stokes vector, S, of the light and the measured Stokes vector, S', follow the relation

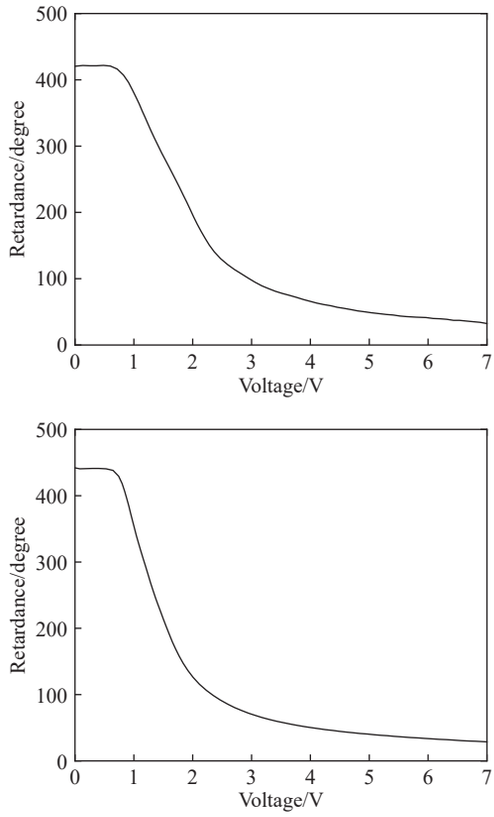


Fig. 4. LCVR retardance calibration curves. The upper panel shows LCVR 1, and the lower panel shows LCVR 2, indicating a nonlinear relationship between applied voltage and generated retardance.

Table 1. The four groups of voltages determined from LCVRs calibration.

LCVR1	Retardance(Â°)	315	315	225	225
	Voltage(V)	1.311	1.311	1.806	1.806
LCVR2	Retardance(Â°)	305.264	54.736	125.264	234.736
	Voltage(V)	1.163	3.658	2.021	1.421

$$S' = M_n \cdots M_2 \cdot M_1 \cdot S = M_i \cdot S, \tag{4}$$

where $M_1 \ldots M_n$ are the Mueller matrices of the optical elements, and M_i is the Mueller matrix of the instrument.

When the linear polarizer of the calibration unit is fixed horizontally ($\theta_p = 0$), and the fast axis of the quarter-wave plate, θ_i, rotates from 0° to 180° in increments of 5°, the input Stokes vector can be described as

$$S_{\text{in}} = M_r(\theta_i) \cdot M_p(\theta_p) \cdot S = \frac{I_0}{2} \begin{pmatrix} 1 \\ \cos^2 2\theta_i \\ \sin 2\theta_i \cos 2\theta_i \\ \sin 2\theta_i \end{pmatrix}. \tag{5}$$

Fig. 5 shows theoretical input values from the calibration unit, the experimentally measured values from the entire system, and the calibrated values obtained using the instrumental Mueller matrix. The Stokes vectors after calibration are in good agreement with the ideal values.

Based on the above formulas and the data shown in Fig. 5, the instrument's Mueller matrix can be calculated as

$$M_i = \begin{pmatrix} 1 & 0 & 0 & 0 \\ 0.028\,8 & 0.974\,2 & 0.066\,7 & 0.011\,3 \\ -0.042\,4 & -0.046\,4 & 0.832\,4 & 0.007\,7 \\ -0.001\,7 & 0.021\,2 & 0.026\,0 & 1.004\,9 \end{pmatrix}. \tag{6}$$

After applying this Mueller matrix to linearly polarized incident light, we compare the calibrated measurement values with the theoretical input values, yielding a Root-Mean-Square (RMS) deviation of approximately 0.3%. After applying the Mueller matrix correction described above, the measurement accuracy for incident linearly polarized light is notably improved.

3.4. The System Contrast

For the Polarimetric Imaging Coronagraph System, after carefully aligning the LCP vortex phase mask in the vortex coronagraph, we installed the polarimetric module directly after the coronagraph in the optical path. We then used custom LabVIEW software to enable synchronized operation of the LCVRs and the CCD, ensuring correct image acquisition during the polarization modulation process, sequentially applying voltage sequences from Table. 1 to the two LCVRs. For every modulation state, the two beams separated by the Wollaston prism were captured by the CCD. The polarization contrast is given by the ratio between the residual starlight PSF in the reconstructed polarization image and the initial starlight PSF[26]. First, we acquired the original PSF image. To avoid image saturation, we used a ND filter with OD = 4, and a shorter exposure time of 5 ms. After aligning and optimizing the entire optical system, we applied four groups of voltages to the two LCVRs, with the only illumination coming from the stellar light. For each voltage setting, we recorded 500–1000 images, with a fixed exposure time to reduce readout noise. All images were dark-frame corrected using a master dark frame calculated from 100 consecutively acquired dark frames. The residual polarized image was obtained through polarization modulation, yielding the Stokes Q component. We derived the final contrast curve of the entire system by comparing the PSF of the demodulated Stokes Q component with the peak intensity of the original stellar PSF.

To further suppress the camera readout noise, we applied a 2×2 pixel binning mode, further improving the achievable contrast. The resulting contrast curve is shown in Fig. 6. The combined system achieves a contrast better than 10^{-9} at an angular distance of $3\lambda/D$, and a mean contrast of 4×10^{-9} over the range from 3 to $10\lambda/D$.

In another test, both the stellar light and the planetary light were simultaneously switched on, with the planetary light simulated using a Thorlabs laser identical to that of the stellar light. To implement the desired polarization state of the planetary light, we installed a polarizer (with an orientation previously calibrated and initially set

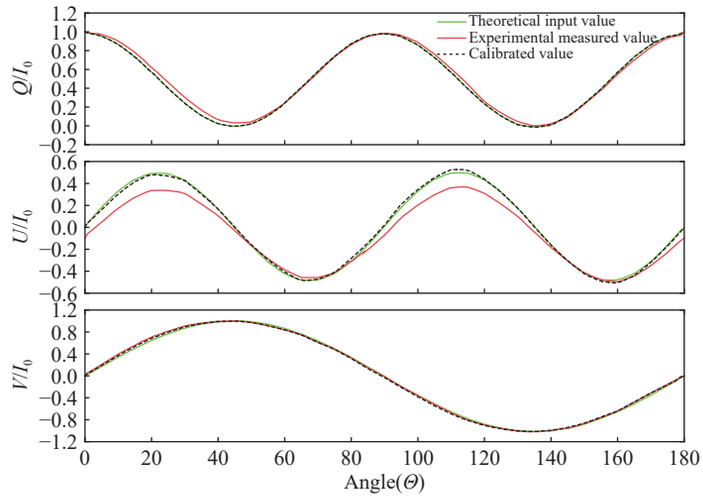


Fig. 5. The calibrated Stokes vectors compared with the theoretical values. The green lines show theoretical input values, while the dashed lines show calibrated values. The calibrated Stokes vectors are in good agreement with the ideal input ones.

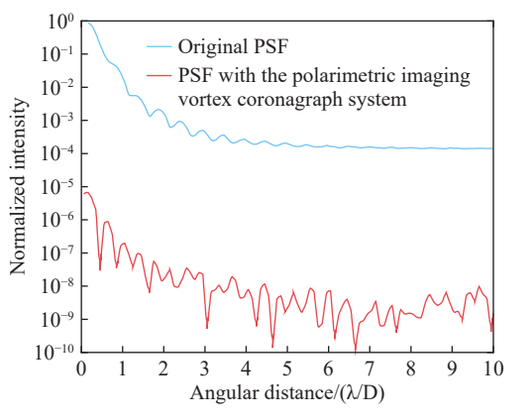


Fig. 6. Experimental contrast curve of the polarimetric imaging coronagraph system. The system achieves a mean contrast of 4×10^{-9} over the range from 3 to $10\lambda/D$.

at 0°) after the laser, producing the intended linear polarization. To calibrate the polarization characteristics of the simulated planetary light, we used the polarimeter to measure its Stokes parameters (I, Q, U, V). The polarizer was then rotated to achieve the target polarization state. For example, when the polarizer was rotated to 45°, the measured Stokes parameters were approximately (1, 0, 1, 0). Subsequently, we calibrated the intensity ratio between the stellar and planetary beams under the same exposure time, by measuring their intensity ratio with the aid of ND attenuation filters. Then, the planetary signal was observed to verify the system performance. The left panel of Fig. 7 shows the original PSF, where the stellar light is dominant and the planetary signal is completely buried. The middle panel shows the PSF after introducing the vortex coronagraph, in which the stellar light is significantly suppressed, although the planetary signal is still not visible to the naked eye. Next, we introduced a polarimeter system downstream of the vortex coronagraph (see Fig. 1 for the complete setup), performing polarimetric detection by applying four different voltage sets to the two LCVRs, with 100–500 images recorded for each voltage set. The images were processed according to the polarization demodulation method described above, and the resulting polarization image clearly reveals the presence of the planet, as shown in the right panel of Fig. 7. The planet is located at approximately 4–5λ/D from the star. The polarimetric differential technique provides an additional contrast improvement of approximately a factor of 100.

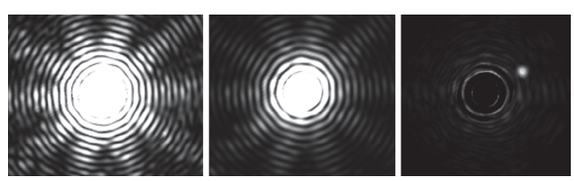


Fig. 7. The original PSF (left), the PSF recorded using the vortex coronagraph (middle), and the image observed after further polarization processing (right).

4. CONCLUSION

In this paper, we present a high-contrast polarimetric imaging vortex coronagraph system. By modulating the focal-plane phase with the vortex phase mask, diffracted stellar light is suppressed, and by adjusting the voltage applied to the LCVRs, their phase retardance can be rapidly tuned, to modulate the incident light. Laboratory experimental results show that the vortex coronagraph achieves a contrast of 10^{-6} at an angular distance of $3\lambda/D$ in the visible band. When combined with the polarimeter, the overall system is capable of providing a contrast of approximately 10^{-9} at small inner working angles across the entire image plane.

The vortex phase mask coronagraph offers a small inner working angle, high optical throughput, and a large discovery area. The dual-LCVR configuration eliminates the need for mechanical rotation and supports both observation and calibration modes. With appropriate modulation, it enables precise control of linear and circular polarization states and allows the measurement of the full set of

Stokes parameters within a single exposure sequence.

ACKNOWLEDGEMENTS

This research was supported by the China Manned Space Project (grants nos. CMS-CSST-201906, CMS-CSST-2025-A18, CMS-CSST-2025-A17) and the National Natural Science Foundation of China (grants nos.11827804 and U2031210).

AUTHOR CONTRIBUTIONS

Jiangpei Dou played a pivotal role in conceptualizing the system framework and methodology. Jing Guo worked on the polarization system. Jiangpei Dou and Jing Guo also reviewed and edited the manuscript. Yutong Cheng was responsible for experimental work, validation, and data processing, and drafted the initial manuscript. All authors read and approved the final version.

DECLARATION OF INTERESTS

The authors declare no competing interests.

REFERENCES

[1] Mayor, M., & Queloz, D. 1995. A Jupiter-mass companion to a solar-type star. *Nature*, **378**(6555): 355−359

[2] Mayor, M., Pepe, F., Queloz, D., et al. 2003. Setting New Standards with HARPS. *The Messenger*, **114**: 20−24

[3] Borucki, W. J., Agol, E., Fressin, F., et al. 2013. Kepler-62: A Five-Planet System with Planets of 1.4 and 1.6 Earth Radii in the Habitable Zone. *Science*, **340**(6132): 587−590

[4] Pepe, F., Cameron, A. C., Latham, D. W., et al. 2013. An Earth-sized planet with an Earth-like density. *Nature*, **503** (7476): 377−380

[5] Liu, C.-C., Ren, D.-Q., Zhu, Y.-T., et al. 2016. A high-contrast imaging polarimeter with a steppedtransmission filter based coronagraph. *Research in Astronomy and Astrophysics*, **16**(5): 73

[6] Guyon, O., Pluzhnik, E. A., Kuchner, M. J., et al. 2006. Theoretical Limits on Extrasolar Terrestrial Planet Detection with Coronagraphs. *Astrophysical Journal*, **167**(1): 81−99

[7] Mawet, D., Riaud, P., Absil, O., et al. 2005. Annular Groove Phase Mask Coronagraph. *The Astrophysical Journal*, **633** (2): 1191−1200

[8] Foo, G., Palacios, D. M., & Swartzlander, Jr., G. A. 2005. Optical vortex coronagraph. *Optics Letters*, **30**(24): 3308−3310

[9] Boccaletti, A., Riaud, P., Baudoz, P., et al. 2004. The Four-Quadrant Phase Mask Coronagraph. IV. First Light at the Very Large Telescope. *Publications of Astronomical Society of the Pacific*, **116**(825): 1061−1071

[10] Delacroix, C., Absil, O., Mawet, D., et al. 2012. A diamond AGPM coronagraph for VISIR. In proceedings of Ground-based and Airborne Instrumentation for Astronomy IV. DOI: *10.1117/12.926494*

[11] Swartzlander, Jr., G. A. 2001. Peering into darkness with a vortex spatial filter. *Optics Letters*, **26**(8): 497−499

[12] Swartzlander, Jr., G. A. 2005. Broadband nulling of a vortex phase mask. *Optics Letters*, **30**(21): 2876−2878

[13] Rouan, D., Baudrand, J., Boccaletti, A., et al. 2007. The Four Quadrant Phase Mask Coronagraph and its avatars. *Comptes Rendus Physique*, **8**(3-4): 298−311

[14] Swartzlander, Jr., G. A., Ford, E. L., Abdul-Malik, R. S., et al. 2008. Contrast Enhancement of Binary Star System Using an Optical Vortex Coronagraph. *arXiv eprints*,, arXiv: 0805.0837.

[15] Berry, M. V. 1987. The Adiabatic Phase and Pancharatnam's Phase for Polarized Light. *Journal of Modern Optics*, **34**(11): 1401−1407

[16] Mawet, D., Serabyn, E., Liewer, K., et al. 2010. The Vector Vortex Coronagraph: Laboratory Results and First Light at Palomar Observatory. *The Astrophysical Journal*, **709**(1): 53−57

[17] Delacroix, C., Absil, O., Forsberg, P., et al. 2013. Laboratory demonstration of a mid-infrared AGPM vector vortex coronagraph. *Astronomy and Astrophysics*, **553**: A98

[18] Absil, O., Mawet, D., Delacroix, C., et al. 2014. The VORTEX project: first results and perspectives. In proceedings of Adaptive Optics Systems IV. DOI: *10.1117/12.2055702*

[19] Bordé, P. J., & Traub, W. A. 2006. High-Contrast Imaging from Space: Speckle Nulling in a Low-Aberration Regime. *The Astrophysical Journal*, **638**(1): 488−498

[20] Dou, J., & Dong, H. 2024. A high-contrast imaging coronagraph for segmented-mirror large aperture telescopes using a spatial light modulator. *Astronomical Techniques and Instruments*, **1**(3): 166−170

[21] Seager, S., Whitney, B. A., & Sasselov, D. D. 2000. Photometric Light Curves and Polarization of Close-in Extrasolar Giant Planets. *The Astrophysical Journal*, **540**(1): 504−520

[22] Stam, D. M., Hovenier, J. W., & Waters, L. B. F. M. 2004. Using polarimetry to detect and characterize Jupiter-like extrasolar planets. *Astronomy and Astrophysics*, **428**: 663−672

[23] Perrin, M. D., Duchene, G., Millar-Blanchaer, M., et al. 2015. Polarimetry with the Gemini Planet Imager: Methods, Performance at First Light, and the Circumstellar Ring around HR 4796A. *The Astrophysical Journal*, **799**(2): 182

[24] Schmid, H. M., Bazzon, A., Roelfsema, R., et al. 2018. SPHERE/ZIMPOL high resolution polarimetric imager. I. System overview, PSF parameters, coronagraphy, and polarimetry. *Astronomy and Astrophysics*, **619**: A9

[25] Xin, Y.-X., Bai, J.-M., Qu, Z.-Q., et al. 2022. YFPOL: A Linear Polarimeter of Lijiang 2.4 m Telescope. *Research in Astronomy and Astrophysics*, **22**(9): 095002

[26] Ren, D., Ranganathan, M., & Christian, D. J. 2019. A Host-star Calibration Based Polarimeter for Earthlike Exoplanet Imaging. *Publications of Astronomical Society of the Pacific*, **131**(1005): 115004

[27] Niv, A., Biener, G., Kleiner, V., et al. 2006. Manipulation of the Pancharatnam phase in vectorial vortices. *Optics Express*, **14**(10): 4208−4220

[28] Palacios, D. M. 2005. An optical vortex coronagraph. In proceedings of Techniques and Instrumentation for Detection of Exoplanets II. DOI: *10.1117/12.617900*

[29] Dou, J., Ren, D., Zhu, Y., et al. 2012. A demonstration test of the dual-beam polarimetry differential imaging system for the high-contrast observation. In proceedings of Ground-

based and Airborne Instrumentation for Astronomy IV. DOI: *10.1117/12.924246*

[30] Dou, J., Ren, D., Zhu, Y., et al. 2012. Laboratory test of a polarimetry imaging subtraction system for the high-contrast imaging. In proceedings of Ground-based and Airborne Instrumentation for Astronomy IV. DOI: *10.1117/12.924245*

[31] Uribe-Patarroyo, N., Alvarez-Herrero, A., Heredero, R. L., et al. 2008. IMaX: a polarimeter based on Liquid Crystal Variable Retarders for an aerospace mission. *Physica Status Solidi C Current Topics*, **5**(5): 1041−1045

[32] Guo, J., Ren, D.-Q., Liu, C.-C., et al. 2017. Design and calibration of a high-sensitivity and high-accuracy polarimeter based on liquid crystal variable retarders. *Research in Astronomy and Astrophysics*, **17**(1): 8

[33] Liu, C.-C., Ren, D.-Q., Zhu, Y.-T., et al. 2017. Design and experimental test of an optical vortex coronagraph. *Research in Astronomy and Astrophysics*, **17**(6): 060

[34] Wu, S.-T., Efron, U., & Hess, L. D. 1984. Birefringence measurements of liquid crystals. *Applied Optics*, **23**(21): 3911−3915

[35] de Juan Ovelar, M., Snik, F., Keller, C. U., et al. 2014. Instrumental polarisation at the Nasmyth focus of the E-ELT. *Astronomy and Astrophysics*, **562**: A8